Fast and accurate machine-learned interatomic potentials for large-scale simulations of Cu, Al, and Ni

A. Fellman,* J. Byggmästar, F. Granberg, K. Nordlund, and F. Djurabekova
Department of Physics, University of Helsinki, P.O. Box 43, FI-00014 Helsinki, Finland

(Received 28 August 2024; revised 3 February 2025; accepted 14 April 2025; published 23 May 2025)

Machine learning (ML) has become widely used in the development of interatomic potentials for molecular dynamics simulations. However, most ML potentials are still much slower than classical interatomic potentials and are usually trained with near-equilibrium simulations in mind. In this work, we develop ML potentials for Cu, Al, and Ni using the Gaussian approximation potential (GAP) method. Specifically, we create the low-dimensional tabulated versions of the potentials, which allow for two orders of magnitude higher computational efficiency than the GAPs, yet similar accuracy, enabling simulations of large multimillion atomic systems. The ML potentials are trained using diverse curated databases of structures and include fixed external repulsive potentials for short-range interactions. The potentials are extensively validated and used to simulate a wide range of fundamental materials properties, such as stacking faults and threshold displacement energies. Furthermore, we use the potentials to simulate single-crystal uniaxial compressive loading in different crystal orientations with both pristine simulation cells and cells containing preexisting defects.

DOI: 10.1103/PhysRevMaterials.9.053807

I. INTRODUCTION

Machine learning (ML) approaches have become increasingly commonplace in the development of interatomic potentials for atomistic simulations. Machine learning interatomic potentials (MLIPs) have shown excellent accuracy compared to traditional analytical potentials [1,2]. Therefore, MLIPs can bridge the gap between *ab initio* methods, such as density functional theory (DFT), and classical analytical models. A growing number of different ML frameworks exist for the creation of interatomic potentials, and the number of available ML potentials is increasing rapidly. ML potentials do not assume fixed functional forms, which allows them to be more flexible than their analytical counterparts, mainly at the cost of computational efficiency. Although numerous different ML potentials for single elements have been developed [3–7], these potentials are usually trained mainly with near-equilibrium simulations in mind. In extreme environments, the simulated systems exhibit far from equilibrium phenomena, and care must be taken to avoid the models breaking down due to the poor extrapolation capability of ML [8]. Additionally, for the Al-Cu alloy system, there exists a Behler-Parrinello neural network potential (NNP), which has been used to study a wide range of materials properties [9].

Molecular dynamics (MD) has been widely used to study the fundamental properties of compressive loading [10–16]. Even though direct comparison between MD simulations and experiments is difficult due to timescale limitations and, therefore, exaggerated strain rates, MD can still provide valuable insights into the fundamental mechanisms with atomic resolution. In particular, MD can provide understanding of the dynamics of dislocation nucleation caused by straining of the materials. Single-crystal compression has been studied extensively in elemental metals with a good portion of the work focusing on Cu. However, most of the simulations are performed on pristine systems without any preexisting defects, even though real materials are never defect-free. In BCC metals, such as tantalum, the effects of preexisting defects on compression has been studied in some detail [17]. There exist some studies of effects of defects on materials response during uniaxial loading of the FCC materials as well [18–22]. However, the defects in these simulations under compressive loading were well defined, such as voids or stacking fault tetrahedra (SFT).

Additionally, it has been shown that the choice of interatomic potential in terms of accuracy is crucial for loading simulations that lead to plastic deformation, i.e., compression, tension, or nanoindentation [23]. In this respect, ML potentials can offer the required accuracy for modeling of these phenomena. However, in large-scale simulations, computational costs may become prohibitively high, limiting the use of the most accurate machine learning potentials. Thus, the development of more efficient, but still sufficiently accurate ML potentials for large-scale simulations (length and time) is highly desirable.

In this work, we train ML potentials for elemental copper, aluminium, and nickel, with the specific focus on large-scale simulations and far-from-equilibrium conditions such as those found in radiation damage events. The potentials are validated and ultimately used to study both the threshold displacement energies as well as single-crystal uniaxial compression. For the compression tests, in contrast to most of the previous studies, we consider the simulation cells with the saturated level of defects. The latter were introduced by means of Frenkel pair insertion with subsequent annealing. This technique allows to obtain uniform distributions of defects of different kind, including point defects, defect clusters, and dislocations.

*Contact author: aslak.fellman@helsinki.fi

Uniaxial compressive loading is then performed along various crystallographic orientations with both the pristine cells and the cells with saturated level of radiation defects.

II. METHODS

A. Gaussian approximation potentials

All potentials presented in this work are Gaussian approximation potentials (GAP) trained with different combinations of descriptors [24]. GAP is a ML framework based on sparse Gaussian process regression and some combination of descriptors for the encoding of local atomic environments. The total energy of models used in this work are defined as

$$E_{\text{tot.}} = E_{\text{rep.}} + E_{\text{ML}}, \tag{1}$$

where the energy of the system is separated into an external repulsive potential, $E_{\text{rep.}}$, and a machine-learned part, E_{ML}, trained as a GAP. The repulsive part is included in order to more accurately describe short-range interactions, as shown in more detail in Ref. [8]. The repulsive part in our case is a Ziegler-Biersack-Littmark-type (ZBL) [25] repulsive potential:

$$E_{\text{rep.}} = \sum_{i<j}^{N} \frac{1}{4\pi\epsilon_0} \frac{Z_i Z_j e^2}{r_{ij}} \phi(r_{ij}/a) f_{\text{cut}}(r_{ij}), \tag{2}$$

where

$$a = \frac{0.46848}{Z_i^{0.23} + Z_j^{0.23}}. \tag{3}$$

The screening function $\phi(r_{ij}/a)$ is not the universal ZBL one, but refitted to repulsive dimer data from all-electron DFT calculations [26]. Additionally, the screened Coulomb potential is multiplied by a cutoff function, $f_{\text{cut}}(r_{ij})$, to force it to zero well below the nearest-neighbor distance of each material, to avoid interfering with the near-equilibrium interactions described by the machine-learned part. The range of the cutoff was chosen to be 1.0–2.2 Å to ensure a smooth transition between the all-electron calculations and short-range DFT data that were part of the training data.

The ML part of the model can be further divided into two-body and many-body terms. For the models referred to in this work as GAP, the total energy is described using the following equation:

$$\begin{aligned} E_{\text{GAP}} = E_{\text{rep.}} &+ \sum_{i<j}^{N} \delta_{\text{2b}}^2 \sum_{s}^{M_{\text{2b}}} \alpha_s K_{\text{se}}(r_{ij}, r_s) \\ &+ \sum_{i}^{N} \delta_{\text{SOAP}}^2 \sum_{s}^{M_{\text{SOAP}}} \alpha_s K_{\text{SOAP}}(\boldsymbol{q}_i, \boldsymbol{q}_s). \end{aligned} \tag{4}$$

Here the sum over N refers to the sum over local descriptor environments and M refers to selected sparsified subset of descriptor environments from training structures. The two-body term consists of prefactors δ_{2b}^2 and regression coefficients α_s. Furthermore, it uses a squared exponential kernel K_{se} and a two-body descriptor that corresponds simply to the distance between two atoms. The many-body term uses the widely known SOAP (smooth overlap of atomic positions) kernel and descriptor [27]. The inner sums in the equation run over sparsified subsets of the reference systems used for the training of the potential.

In addition to the GAP (with the SOAP descriptor), we created low-dimensional tabulated versions (tabGAP) of the ML potentials [28,29]. The total energy for the tabGAP is defined similarly as for the model described in Eq. (4), but with a different selection of descriptors:

$$\begin{aligned} E_{\text{3b+eam}} = E_{\text{rep.}} &+ \sum_{i<j}^{N} \delta_{\text{2b}}^2 \sum_{s}^{M_{\text{2b}}} \alpha_s K_{\text{se}}(r_{ij}, r_s) \\ &+ \sum_{i,j<k}^{N} \delta_{\text{3b}}^2 \sum_{s}^{M_{\text{3b}}} \alpha_s K_{\text{se}}(\boldsymbol{q}_{ijk}, \boldsymbol{q}_s) \\ &+ \sum_{i}^{N} \delta_{\text{eam}}^2 \sum_{s}^{M_{\text{eam}}} \alpha_s K_{\text{se}}(\rho_i, \rho_s) \end{aligned} \tag{5}$$

Whereas the model in Eq. (4) uses the SOAP descriptor, the tabGAP potential uses a three-body cluster descriptor (defined as a three-valued permutation-invariant vector [30]) and an embedded atom method (EAM) density descriptor. The EAM density is a scalar pairwise summed radial function, as in standard EAM potentials [28,31,32]. Cutoff functions are applied on the kernels to limit the interaction range. No inner cutoffs are applied, but for short interatomic distances the contributions from the ML terms are negligible compared to the repulsive potential $E_{\text{rep.}}$ [8].

The tabGAP potential is trained similarly as the GAP potential, but after the initial training of the model, the energy contributions of the different terms of the potential are tabulated onto low-dimensional grids and evaluated using cubic-spline interpolation. The repulsive and two-body terms are tabulated into a one-dimensional grid, the three-body term into a three-dimensional grid and the EAM term into two one-dimensional grids. With dense enough grid sampling, the interpolation errors are negligible [33]. Further details on the tabulation process can be found in Refs. [28,29]. The simpler descriptors of the tabGAP model allows for this tabulation, which while sacrificing a little accuracy compared to SOAP-GAP gives the model a two-orders-of-magnitude increase in computational efficiency from the GAP, making the model more suitable for large-scale simulations. Furthermore, previous work using the tabGAP formalism in BCC high-entropy alloys has demonstrated good extendability of the method with increased number of chemical species [28].

B. Density functional theory calculations

All the DFT calculations in this work were performed using the VASP DFT code [34–37]. The calculations used the PBE GGA exchange-correlation function [38] and projector augmented wave (PAW) pseudopotentials (Cu_pv, Al, Ni). The plane-wave expansion energy cutoff was 500 eV for all elements. K points were defined using Γ-centered Monkhorst-Pack grids [39] with maximum k spacing of 0.15 Å^{-1}. Additionally, first-order Methfessel-Paxton smearing of 0.1 eV was applied [40]. For Ni, collinear spin-polarized calculations with initialized ferromagnetic order were performed, while the Cu and Al calculations did not include spin polarization. We employ spin polarization for Ni as this makes it easier

to combine its DFT data in the future with alloying elements where magnetism might become relevant. Furthermore, the magnetic moment after a simple relaxation in FCC Ni was about $0.6\,\mu_B$ per atom. Parameters such as energy cutoff, k spacing, and smearing were kept the same for all calculations and elements in order to allow for the possibility to combine data between elements for the creation of alloy potentials in the future.

C. Training and testing data

Like in most ML applications, the quality of the training data is critical for the quality of the final model. The training data should reflect the expected range of circumstances that can reasonably occur during the use of the model. The potentials presented in this work were designed with the goal of making a good general-purpose model with additional considerations for short-range repulsive interactions, which take place in far-from-equilibrium simulations, such as radiation damage simulations. We note that the database has been constructed for a general-purpose model with no specific simulation type in mind. In the latter case, the applicability of the potential must be additionally validated, since tailored models may still be required in some cases. The training data consist of the following classes of structures:

(1) Randomly distorted unit cells (FCC, BCC, and HCP).

(2) FCC, BCC, and HCP lattices at finite temperatures and different volumes, initially created by running MD simulations with earlier iterations of the final potentials.

(3) Systems containing various small vacancy and interstitial clusters (from one to three defects with different configurations).

(4) Liquid systems with various densities prepared by melting MD simulations.

(5) (1 0 0), (1 1 0), and (1 1 1) FCC surfaces.

(6) Structures with a few disordered surface layers.

(7) Stacking-fault-like structures where a small slab is moved on a atom plane randomly.

(8) Dimers and trimers with various distances between atoms.

(9) Short-range systems, where an atom is randomly inserted into an FCC lattice fairly close to other atoms ($\geqslant 1$ Å).

(10) Structures with trajectories of a single atom being moved along a rigid path in various high-symmetry directions while the other atoms remained fixed.

The training datasets for the GAP and tabGAP were kept identical. However, there are slight differences between the different DFT databases for the different elements. The Al potentials do not include dimers as the inclusion of the dimer data degraded the accuracy and computed properties of the potentials. Likewise, for Cu and Ni trimers were omitted from their respective training databases, due to similar concerns. This degradation came mostly in the form of overfitting issues to the high-energy structures included in the dimers and trimers and affected especially the elastic properties and formation energies. This is mostly due to the challenging structures we wanted to include into the training data for nonequilibrium properties. These detrimental effects can be mitigated by hyperparameter tuning and by careful curation of the training data, but ultimately the omission of certain structures yielded best results in our case. Before training, a random subset (5%–10%) of the training data containing systems from each category was removed and put aside and used as testing datasets.

TABLE I. Hyperparameters used for the different descriptors: cutoff radius r_{cut}, width of the cutoff region $r_{\Delta\text{cut}}$, energy prefactor δ, and the number of sparse descriptor environments from the training structures M.

Formalism	Descriptor	r_{cut}(Å)	$r_{\Delta\text{cut}}$(Å)	δ	M
	2b	5.2	1.0	10	20
tabGAP	EAM	5.2	1.0	1.0	20
	3b	4.0 (4.5 Al)	0.6	1.0	700
GAP	2b	5.2	1.0	10	20
	SOAP	4.5	1.0	2.0	2000

D. Hyperparameters

The GAPs described here have a number of hyperparameters that have to be set before training. Table I shows the hyperparamaters used for the different descriptors. The cutoff distance of the three-body descriptor for Al was chosen to be longer, as Al has a significantly larger lattice constant. The results showed that, indeed, the longer cutoff in case of Al improved the model accuracy for this material. Additionally, the SOAP descriptor used 8 as the number of radial basis functions (n_{max}) and number of spherical harmonic (l_{max}). Another set of hyperparameters are the regularization terms σ for the energies, forces and virials. The default values for these parameters were 1 meV/atom, 0.04 eV Å^{-1} and 0.1 eV, respectively. For systems such as liquid structures, dense structures, and short-range interactions (including trajectories) these regularization terms were increased by a factor of 10 (10σ). The sparse sampling used CUR (datapoints) for the SOAP descriptor, while all other descriptors in this work used uniform sampling as implemented in the GAP framework. The number of grid points used in the tabulation was chosen after convergence testing to be 5000 for both two-body and EAM descriptors and for the three-body grid to be $80 \times 80 \times 80$.

E. Threshold displacement energy calculations

All MD simulations in this work were done using the LAMMPS simulation package [41]. The threshold displacement energies were determined by sampling 800 random spherically uniformly distributed lattice directions. A series of simulations were performed for each direction, where an atom is given higher and higher kinetic energy (2 eV increments) in the specific direction until a stable defect is formed. During this simulation, border cooling was applied (NVT) with a temperature of 10 K, while the rest of the system was kept in the NVEensemble. The simulation cell was chosen to be $(12 \times 13 \times 14)$ units cells which corresponds to 8736 atoms. A noncubic simulation cell size was specifically chosen to reduce the possibility that replacement collision sequences along low-index crystal directions interact with themselves across the periodic boundaries.

F. Uniaxial compressive loading

For the uniaxial compressive loading simulations, cells in two crystal orientations were created: one with the ⟨1 0 0⟩ lattice orientation aligned with the z axis and one with ⟨1 1 1⟩ alignment. Furthermore, for each direction, a simulation cell containing defects was created in addition to the pristine bulk cells. All side lengths of the simulation cells were roughly equal, and they were around 22–27 nm in length depending on element and orientation. This corresponds to a system size of around 1.1 million atoms. These simulation cells were large enough for imaging effects from periodic boundary conditions to be negligible [12]. The pristine systems were thermalized to 300 K in NPT conditions for 60 ps. The simulation cells containing defects were created from the pristine cells by manually inserting around 10 000 randomly placed Frenkel pairs (FPs) into the cell. The created structures were then minimized using the conjugate gradient method in order to ensure that atoms were not accidentally moved too close to each other during the insertion of FPs. The cells were then heated up from 100 K to 300 K in theNPT ensemble for 200 ps after which the system was additionally relaxed for 400 ps at the 300 K temperature in the same NPT ensemble. The final configurations were periodic in all directions and were used as starting points for the uniaxial loading simulations. The compression simulations were performed by uniaxial compressive loading of a given orientation with a constant strain rate of 1×10^8/s. This strain rate has been used in previous studies and shown to be sufficiently low with a negligible effect on the maximal yield stress [11]. The directions orthogonal to the loading direction were decoupled from the latter and the temperature and pressure in these directions were controlled in the NPT ensemble. The temperature of the system was kept at 300 K and a 0.001 ps time step was used in all simulations. During compression the stresses were calculated from the per-atom stresses of all the atoms in the system and the atomic configurations were stored at regular intervals. This procedure was continued until the maximal strain of 20% was reached.

III. RESULTS AND DISCUSSION

A. Train and test errors

Table II shows the root-mean-square (RMS) errors of the testing data of each potential. Overall the errors show that the simpler descriptors of tabGAP only slightly reduces the accuracy in regards to energy and force errors compared to GAP with the SOAP descriptor. The largest difference between GAP and tabGAP is seen for Ni, but the RMS errors of the Ni tabGAP are still low, a few meV/atom, and hence acceptable. Furthermore, we divide here the testing data into crystalline and liquid structures in order to highlight the difference between them, as liquids and disordered structures are in general more difficult to describe.

B. Computational efficiency

Computational efficiency was measured by running simulations containing 32 000 atoms with the different interatomic potentials. All simulations were done on a single Xeon Gold 6230 CPU core. Table III shows the benchmarking results of different potentials (smaller number equals to a more computationally efficient potential). We can clearly see that tabGAP is about 80–150 times faster than its GAP counterpart. In recent years significant developments have been made in the computational efficiency of ML potentials with methods such as neural network potentials (NNP) and atomic cluster expansion which show significant improvements in performance and computational efficiency compared to GAP [4,5]. Furthermore, we compare computational efficiency of the presented models with the recent implementation of the atomic cluster expansion (PACE) model as it has been shown to be the best performing in terms of accuracy and efficiency [5]. Compared with the PACE model the tabGAP potential is about 17 times faster. Furthermore, we compare against the Al-Cu Behler-Parrinello neural network potential (NNP11) [9], where we can also see an order of magnitude difference compared to tabGAP. Additionally, the tabGAP potential is only an order of magnitude slower than classical EAM potentials, which is a reasonable increase of computational costs given the higher accuracy and the consistency with DFT calculations of the ML models compared to the EAM ones.

TABLE II. Energy E and force F RMS errors of the testing data for crystalline and liquid structures separately.

		(meV/atom)		(eV/Å)	
		$E_{\text{crystalline}}$	E_{liquid}	$F_{\text{crystalline}}$	F_{liquid}
Cu					
	GAP	0.8	3.0	0.015	0.06
	tabGAP	1.1	2.0	0.015	0.03
Al					
	GAP	0.6	2.4	0.014	0.06
	tabGAP	1.1	3.0	0.02	0.06
Ni					
	GAP	0.5	1.9	0.012	0.1
	tabGAP	1.6	3.9	0.07	0.12

C. Basic material properties

To verify the accuracy of the developed potentials, we calculated different material properties. Table IV shows the good agreement with the available DFT and experimental data of the basic structural, elastic, and defect properties obtained with the tabGAP and GAP. Generally, we observe minor differences between the GAP and tabGAP potentials, mainly in the formation energies of defects and elastic constants. The largest difference can be seen in the migration energies of interstitial defects where the GAP model is closer to the

TABLE III. Benchmark of computational efficiency. Computational efficiency given as milliseconds/(atom × step). All simulations are run on a single CPU core with a system containing 32 000 atoms.

	GAP-SOAP	tabGAP	EAM	MLIP
Cu	3.7	0.029	0.0014 [42]	0.51 [5], 0.33 [9]
Al	2.2	0.028	0.002 [43]	0.77 [9]
Ni	4.3	0.029	0.0036 [44], 0.002 [45]	—

TABLE IV. Calculated material properties compared with DFT and experimental results. a: lattice constant (Å); E_{coh}: cohesion energy (eV); $E_{\Delta_{\mathrm{lattice}}}$: energy difference between relaxed structure of given type compared with FCC (meV/atom); $E_{\mathrm{mig}}^{\mathrm{def}}$: defect migration energy in FCC (eV); C_{ij}: elastic constants (GPa); $\gamma_{(hjk)}$: surface energies (mJ/m^2); E_{f}: formation energy of a single vacancy and interstitials (eV); T_{melt}: melting temperature (K).

		GAP	tabGAP	DFT	Expt.
Cu					
	a	3.626	3.625	3.632	3.615 [51]
	E_{coh}	3.724	3.724	3.724	3.49 [51]
	$E_{\Delta_{\mathrm{bcc}}}$	38.2	37.9	36.3	—
	$E_{\Delta_{\mathrm{hcp}}}$	7.9	8.0	7.5	—
	$E_{\mathrm{mig}}^{\mathrm{vac.}}$	0.742	0.780	0.79 [4]	0.70 [52–54]
	$E_{\mathrm{mig}}^{\mathrm{SIA}}$	0.121	0.155	—	0.117 [52–54]
	C_{11}	163	168	166	169 [50]
	C_{12}	122	138	119	122 [50]
	C_{44}	77	81	76	75 [50]
	$\gamma_{(100)}$	1470	1486	1470 [46]	1520 (no specific direction), [47]
	$\gamma_{(110)}$	1556	1558	1560 [46]	—
	$\gamma_{(111)}$	1321	1326	1340 [46]	—
	$E_{\mathrm{f}}^{\mathrm{vac}}$	0.92	1.03	1.08	1.28 ± 0.05 [50]
	$E_{\mathrm{f}}^{\mathrm{100d}}$	2.95	3.04	3.22	2.82–4.12 [50]
	$E_{\mathrm{f}}^{\mathrm{octa}}$	3.36	3.36	3.51	—
	$E_{\mathrm{f}}^{\mathrm{tetra}}$	3.56	3.59	3.90	—
	T_{melt}	1270	1250	—	1356 [49]
Al					
	a	4.040	4.041	4.043	4.050 [50]
	E_{coh}	3.695	3.695	3.693	3.39 [51]
	$E_{\Delta_{\mathrm{bcc}}}$	93.1	93.3	88.7	—
	$E_{\Delta_{\mathrm{hcp}}}$	28.5	28.7	29.2	—
	$E_{\mathrm{mig}}^{\mathrm{vac.}}$	0.527	0.534	0.30–0.63 [55]	0.61 [52–54]
	$E_{\mathrm{mig}}^{\mathrm{SIA}}$	0.097	0.065	—	0.112–0115 [52–54]
	C_{11}	105	101	101	108 [50]
	C_{12}	63	70	66	62 [50]
	C_{44}	32	37	29	28 [50]
	$\gamma_{(100)}$	900	897	910 [46]	1140 (no specific direction), [47]
	$\gamma_{(110)}$	985	975	980 [46]	—
	$\gamma_{(111)}$	772	810	770 [46]	—
	$E_{\mathrm{f}}^{\mathrm{vac}}$	0.67	0.66	0.68	0.67 ± 0.03 [50]
	$E_{\mathrm{f}}^{\mathrm{100d}}$	2.63	2.66	2.66	3.0 [50]
	$E_{\mathrm{f}}^{\mathrm{octa}}$	2.83	2.84	2.88	—
	$E_{\mathrm{f}}^{\mathrm{tetra}}$	3.16	3.15	3.23	—
	T_{melt}	910	870	—	933 [49]
Ni					
	a	3.518	3.518	3.519	3.524 [50]
	E_{coh}	4.715	4.715	4.713	4.44 [51]
	$E_{\Delta_{\mathrm{bcc}}}$	94.6	94.7	98.3	—
	$E_{\Delta_{\mathrm{hcp}}}$	27.8	27.6	31.9	—
	$E_{\mathrm{mig}}^{\mathrm{vac.}}$	1.0	1.06	1.12 [4]	1.04 [52–54]
	$E_{\mathrm{mig}}^{\mathrm{SIA}}$	0.157	0.127	—	0.15 [52–54]
	C_{11}	279	281	273	247 [50]
	C_{12}	153	156	155	153 [50]
	C_{44}	125	125	131	122 [50]
	$\gamma_{(100)}$	2213	2208	2210 [46]	1940 (no specific direction), [47]
	$\gamma_{(110)}$	2265	2272	2290 [46]	—
	$\gamma_{(111)}$	1910	1910	1920 [46]	—
	$E_{\mathrm{f}}^{\mathrm{vac}}$	1.46	1.47	1.49	1.79 ± 0.05 [50]
	$E_{\mathrm{f}}^{\mathrm{100d}}$	4.13	4.13	4.07	—
	$E_{\mathrm{f}}^{\mathrm{octa}}$	4.36	4.35	4.26	—
	$E_{\mathrm{f}}^{\mathrm{tetra}}$	4.73	4.73	4.67	—
	T_{melt}	1690	1690	—	1726 [49]

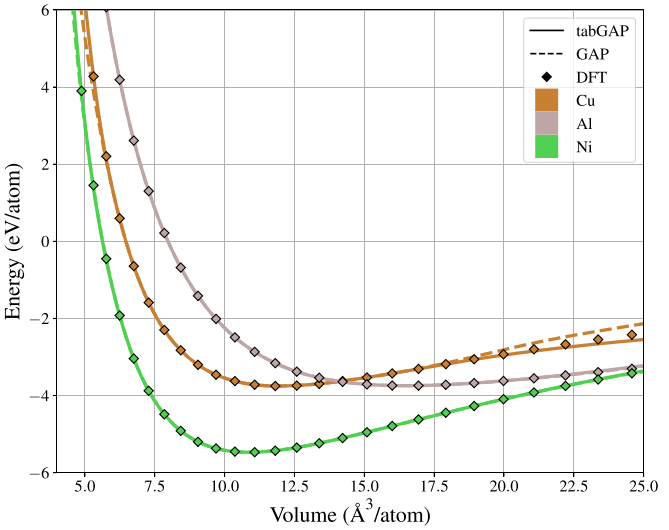

FIG. 1. Energy vs volume compared with DFT calculations for all the potentials in FCC structure.

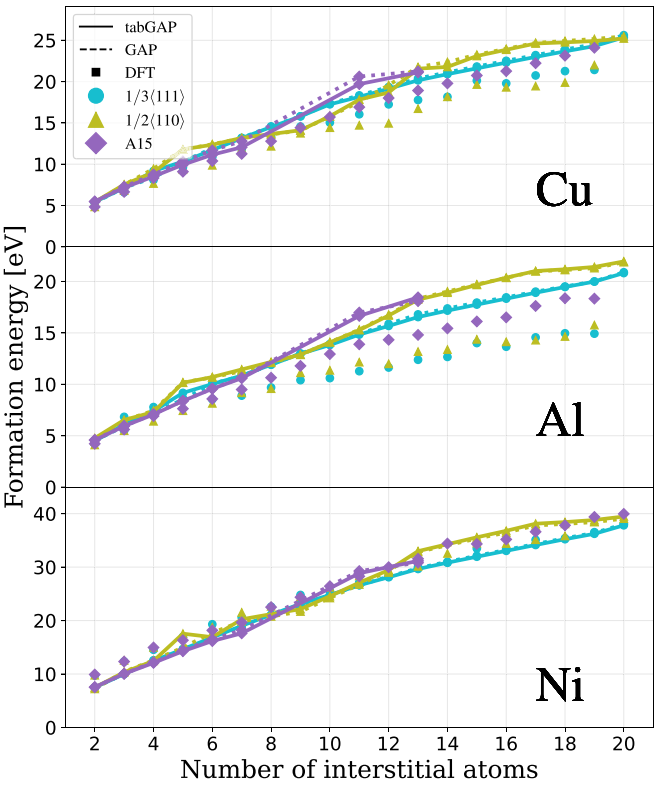

FIG. 3. Defect formation energies of A15 clusters and interstitial dislocation loops compared with DFT calculations (lowest energy data points only) from Ref. [57]. Markers and line styles indicate the method used, and the colors indicate the defect type.

experimental reference compared to tabGAP. The Cu and Al potentials slightly underestimate the formation energies of defects compared to the DFT calculations, while the Ni potentials slightly overestimate them. The surface energies show excellent agreement with the DFT calculations [46]. Furthermore, the agreement with experimental surface energies is good, while it must be noted that experimental values are not for any specific direction and that there is some spread in experimental values [47]. The melting point was estimated using the two-phase method [48] with 20 K temperature increments. It should be noted that in general, the ML potentials slightly underestimate the experimental melting temperatures [49].

In Fig. 1 the energy-volume curves are shown for each of the elements. Here we see an excellent agreement with DFT calculations in a wide range of atomic volumes. In particular, we are interested in validating that the potentials reproduce the repulsive interactions correctly and that there is a smooth transition to the external repulsive potential. The external repulsive potential is added to describe the interactions at very short interatomic distances. However, undesirable issues can still occur in the transition region, where the repulsive potential starts to dominate, especially if the short-range interactions are not properly taken into account. In the case of the Cu GAP potential, we can see some deviations that appear at larger volumes, which are analogous to those reported for other GAP potentials [5]. The energy-volume curves for BCC and HCP phases of the materials under the study can be found in the Supplemental Material [56] Fig. S1, and the accuracy of those is essentially the same as for the FCC case.

We also calculated the phonon dispersion curves for each element in the FCC phase and compared with the available experimental measurements, as shown in Fig. 2. The agreement between GAP, tabGAP, and experiment is excellent for all three materials. This further confirms that the developed potentials can accurately capture elastic and thermal properties of the materials.

Recently, studies into the A15 Frank-Kasper nanophases have shed new light into the formation of dislocation loops

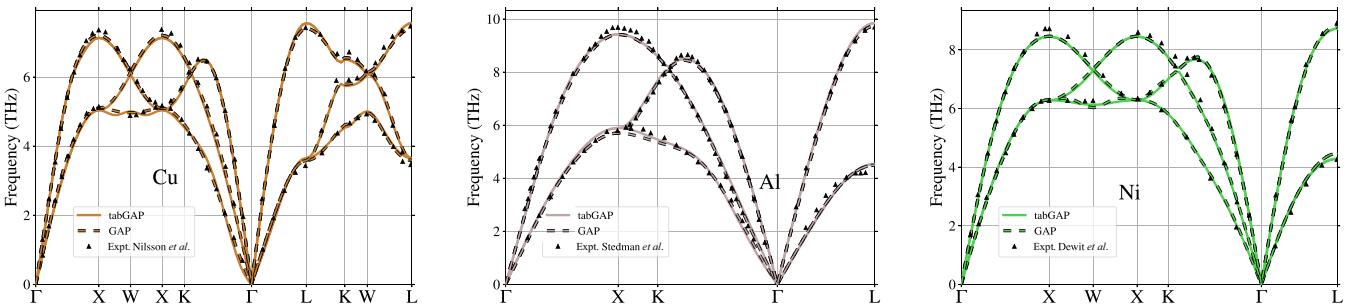

FIG. 2. Phonon dispersion curves calculated using the small displacement method compared to experimental results [59–61].

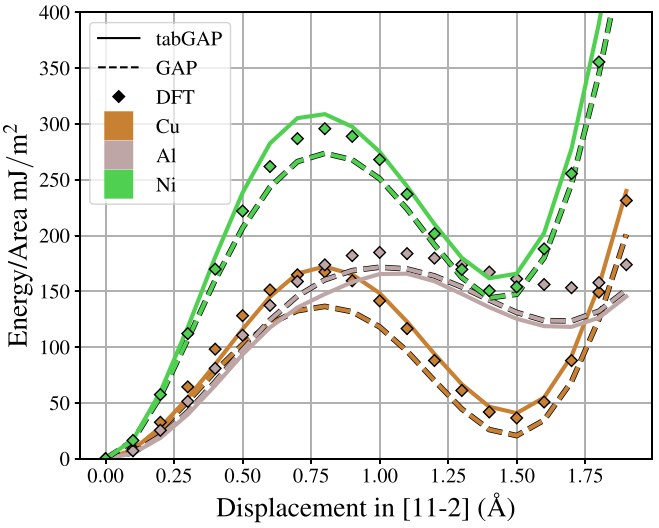

FIG. 4. Generalized stacking fault energy curves calculated with the developed ML potentials and DFT.

in FCC metals [57,58]. Figure 3 shows the defect formation energies of A15 clusters and interstitial-type dislocations compared with DFT calculations from Ref. [57]. The A15 structures were constructed to be the low-energy structures predicted and detailed in Ref. [57]. Additionally, the calculation of formation energies followed closely the methodology detailed in the publication, with system size of $13\,500 + N$, where N is the number of interstitials. Conjugate gradient relaxation was performed with a 0.002 eV/Å force convergence criterion. We can see from Fig. 3 that the results from the GAP and tabGAP potentials are virtually identical. The smaller A15 clusters ($N \leqslant 7$) are in most cases the lowest in energy compared to the two different dislocations for both tabGAP and GAP potentials, while at larger sizes the dislocations are energetically favorable. Interestingly, there are differences between the elements when comparing against the DFT calculations from Ref. [57], where Ni is very similar in magnitude, Cu is slightly higher compared to DFT and for Al this difference is most clear. Note that no A15 clusters or dislocation loops were included in the training database.

The generalized stacking fault energy (GSFE) curves shown in Fig. 4, were calculated by displacing one of the $\{1\,1\,1\}$ slip planes in a $\langle 1\,1\,2\rangle$ direction. The DFT results were calculated for the same systems as with the ML potentials, using the parameters described in Sec. II B without relaxation. A good description of stacking faults is important for the simulation of dislocations and grain boundaries. We also observe a good agreement between the potentials and the DFT results. The GAP potentials predict consistently lower stacking fault energies compared to tabGAP and DFT. Somewhat worse agreement is observed for Al, where both GAP and tabGAP underestimate the GFSE value compared to the DFT calculations. Table V shows the stable stacking fault (marked with the subscript "sf") and unstable stacking fault (marked with the subscript "usf") energies compared to the DFT and experiments. The unstable stacking fault energies of Ni and Cu in GAP are somewhat lower in comparison to those in tabGAP and DFT.

D. Dislocation core structures

We investigated the predicted core structures of edge and screw $a\langle 110\rangle/2$ dislocations using the energy minimization method. The dislocations were introduced into a cylindrical cell following the procedure detailed in Ref. [71]. The radius of the cylinder was $50 \times b$, where b is the Burgers vector length, with an additional 20 Å annular border region. The atoms in the systems were initially displaced according to anisotropic elasticity. After this a conjugate gradient minimization is performed on the system, while fixing the border atoms in place. Atomic illustrations of the minimized dislocation cores from the tabGAP potentials are shown in Fig. 5.

As a result after the minimization procedure, all the initially introduced perfect dislocations dissociated. Although first-principles calculations of dislocation cores remain challenging [72], some approximately comparable DFT calculations have been performed in Al and Ni [73,74]. Interestingly, in some simulations the tabGAP Al screw dislocation did not dissociate during the minimization (Supplemental Material [56] Fig. S2). Previously, a metastable nondissociated core structure of a screw dislocation has been predicted in Al in orbital-free DFT calculations. This was suggested to play a role in the discrepancy of measurements of the Peierls stress for FCC dislocations [75]. However, it is unclear whether the nondissociated state observed in this work is an artifact of the Al tabGAP potential or a feature correctly captured by the

TABLE V. Simulated and experimental values for intrinsic stacking fault energies (γ_{sf}) and unstable stacking fault energies (γ_{usf}) for the created potentials.

		GAP-SOAP	tabGAP	DFT	Expt.
Cu					
	γ_{sf} (mJ/m^2)	20	40	35 (this work), 39 [62], 39 [63], 41 [64]	41 [69], 45 [65,68]
	γ_{usf} (mJ/m^2)	136	170	167 (this work), 158 [63], 164 [62], 180 [64]	
Al					
	γ_{sf} (mJ/m^2)	122	117	153 (this work), 134 [64], 140 [62], 158 [63]	120 [66], 150 [67], 166 [68]
	γ_{usf} (mJ/m^2)	168	158	182 (this work), 169 [64], 177 [62], 175 [63]	
Ni					
	γ_{sf} (mJ/m^2)	145	161	150 (this work), 137 [70], 145 [62]	125 [68]
	γ_{usf} (mJ/m^2)	274	308	296, and 278 (this work), 289 [62]	

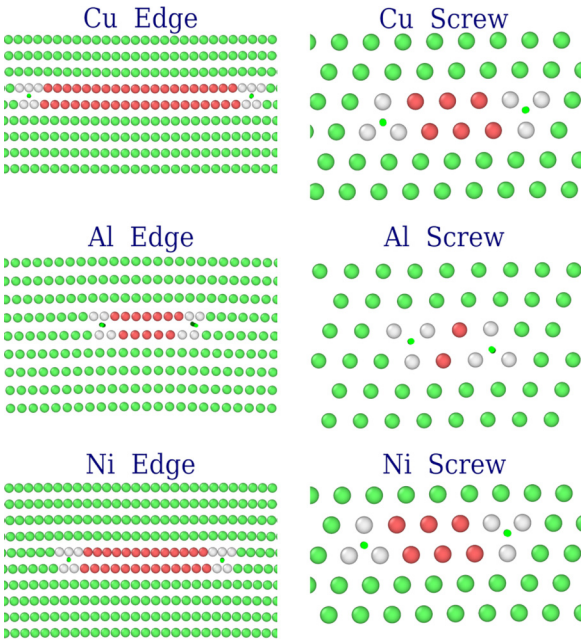

FIG. 5. Dissociated dislocation cores of $a\langle 110\rangle/2$ dislocations after minimization using the tabGAP potentials. Coloring is according to common neighbor analysis: green atoms are FCC, red HCP, white unidentified atoms, and the small green dots the positions of dislocation lines according to DXA analysis [76].

tapGAP, since this metastable state was not observed in either the GAP or the EAM potential.

For a quantitative comparison, we report in Table VI the dissociation distances obtained by different methods. In general, the agreement is reasonable. However, in the case of Cu, the tabGAP results in somewhat lower values of the dissociation distance as compared to the GAP values. Overall, we see that the dissociation distances in Cu are systematically more compact in tabGAP while somewhat broader in GAP as compared to the values reported in the literature.

E. Equation of state

Further validation of the developed potentials versus experiment can be done by comparing the equation of states, as measured in experiment and simulated using the potentials. Figure 6 shows the pressure-volume relation calculated with various potentials compared with experimental data. From the figure we see that the tabGAPs can reproduce very well the experimental results. Although the agreement with experiment is also good for the potentials previously developed for Al and Cu, the results for Ni in different classical EAM potentials agree to much lesser extent with experiment, especially for higher compression. The good agreement of tabGAP results with experiment for this material is encouraging, since an accurate response to pressure is important for extreme environment simulations, such as the uniaxial compressive loading presented in Sec. III H.

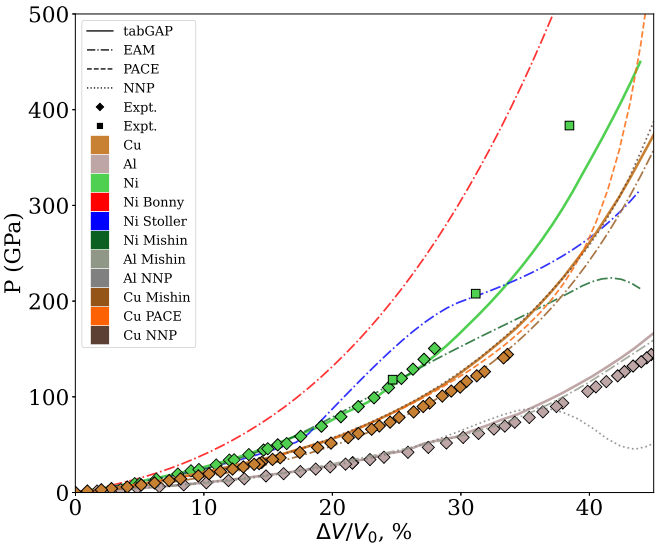

FIG. 6. Equation of state calculated with various different interatomic potentials compared to experimental data (Ni [82], Cu, and Al [83]). The different markers for experimental data for Ni are from different experiments [84,85]. Comparison is made to previously developed potentials: EAM [42–45], PACE [5], Al-Cu NNP11 [9].

F. Threshold displacement energies

The threshold displacement energy (TDE) defines the minimum energy required to displace an atom from its lattice position, creating a stable defect. This is a key parameter for experimental damage dose estimation when using the NRT equation [86]. Moreover, the accuracy of the TDE values predicted by the interatomic potential is important for

TABLE VI. Dissociation distances estimated from different methods (Å). The dissociation distances from this work are estimated from the distance between dislocation lines predicted by DXA [76].

		GAP	tabGAP	EAM [42,43]	Literature
Cu					
	Edge	46.6	28.8	35.5	38.6 [77] (MLIP), 38 ± 6 [69] (DFT)
	Screw	16.7	10.0	12.1	15.7 [77] (MLIP), 18 ± 6 [69] (Expt.)
Al					
	Edge	12.4	11.4	13.3	15.0 [78] (MLIP), 9.5 [73], and 12.8 [79] (DFT)
	Screw	6.5	6.5	6.2	8.6 [78] (MLIP), 7.5 [73], and 8.2 [80] (DFT)
Ni					
	Edge	18.0	19.3	23.0	19.3 [81] (MLIP), 26 ± 8 [65] (Expt.)
	Screw	8.8	9.8	11.9	11.8 [81] (MLIP), 12.0 [74] (DFT)

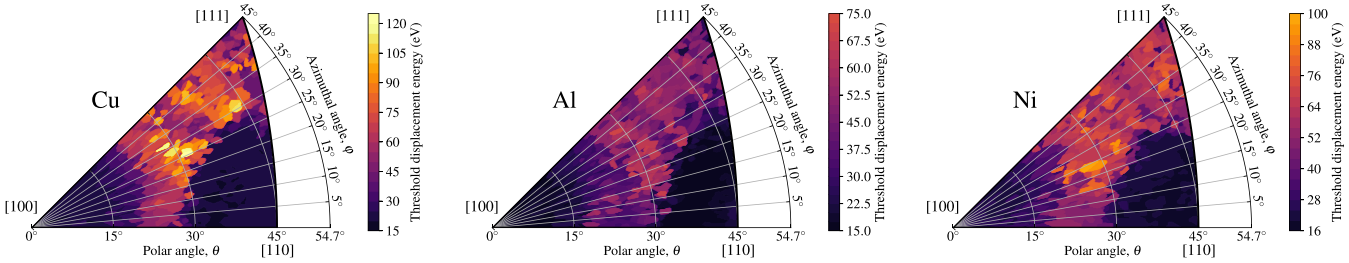

FIG. 7. Threshold displacement energy as a function of PKA direction. The same color range (10–120 eV) is used for all materials.

radiation damage simulations since they correlate directly with the amount of defects produced in cascade events [87,88]. We have calculated the TDEs as a function of lattice direction for each element with the tabGAP potentials; see Fig. 7. Table VII shows the TDEs for some high-symmetry directions of the lattice as well as the average TDE over all directions. Additionally, for the GAP potentials only high-symmetry directions were considered as the full TDE map would have been prohibitively computationally expensive. In this case, 10 runs were initialized with random directions within a 5° cone of each high-symmetry direction. The TDEs predicted for the high-symmetry directions are in good agreement with experimental results. Comparison with the *ab initio* MD results [89] shows that the tabGAP predicted TDE values are consistently lower, but closer to experiment than the *ab initio* MD values. The Al tabGAP potential has a somewhat higher average TDE when comparing with the previous MD results (17–27 eV) for both EAM and MEAM potentials and a more recent deep-learning potential [90]. The ASTM recommends as the effective TDEs 30, 25, and 40 eV for Cu, Al, and Ni, respectively [91]. The calculated averages for the tabGAP potentials are consistently higher than the ASTM recommended values, while still in fairly good agreement. Since the accuracy of the reproduced key properties of materials is overall very similar in tabGAP and GAP, and considering the much lower computational cost of the simulations with tabGAP, hereafter we only calculate and include results obtained with the tabGAPs.

TABLE VII. Threshold displacement energy (eV) for high symmetry directions (±1 eV) and the average (with standard errors). Values given inside parentheses are the averages of the data points within a 5° cone from the specific direction.

	tabGAP	GAP	AIMD	Expt.
Cu				19 [93]
⟨1 0 0⟩	19 (20.3)	19 (19.4)	25 [89]	19 ⟨1 0 0⟩ [92]
⟨1 1 0⟩	21 (22.4)	21 (21.2)		19 ⟨1 1 0⟩ [92]
⟨1 1 1⟩	31 (52.2)	29 (34.8)		
(avg.)	44.4 ± 0.8		29 [94], 43±4 [93]	
Al				16 [93]
⟨1 0 0⟩	15 (17)	17 (17.0)	19 [89]	
⟨1 1 0⟩	17 (19)	15 (18.4)		
⟨1 1 1⟩	19 (37.5)	21 (29.2)		
(avg.)	34.3 ± 0.6			27 [94], 66 ±12 [93]
Ni				23 [93]
⟨1 0 0⟩	21 (23.3)	19 (20.6)	27 [89]	
⟨1 1 0⟩	19 (19.5)	21 (21.4)	30 [89]	21 ⟨1 1 0⟩ [92]
⟨1 1 1⟩	29 (58.6)	29 (39.0)	70 [89]	
(avg.)	42.9 ± 0.7			33 [94], 69 [93]

G. Frenkel pair insertion

To verify the stability of the potential as well as investigate the microstructure of defects predicted by the tabGAPs, we now study the dynamics of the system with high concentration of vacancies and interstitials via insertion of large numbers of randomly created Frenkel pairs, which was followed by MD relaxation runs. During the simulations, the number of vacancies was tracked using the Wigner-Seitz (WS) analysis [95]. Additionally, DXA dislocation analysis [76] as implemented in OVITO [96] was performed to find the types of dislocations present in the simulation cell after relaxation.

Figure 8 shows the evolution of the number of vacancies identified by WS analysis during relaxation. The initial drop of the number of defects is explained by the relaxation of unstable manually inserted defects during the initial relaxation

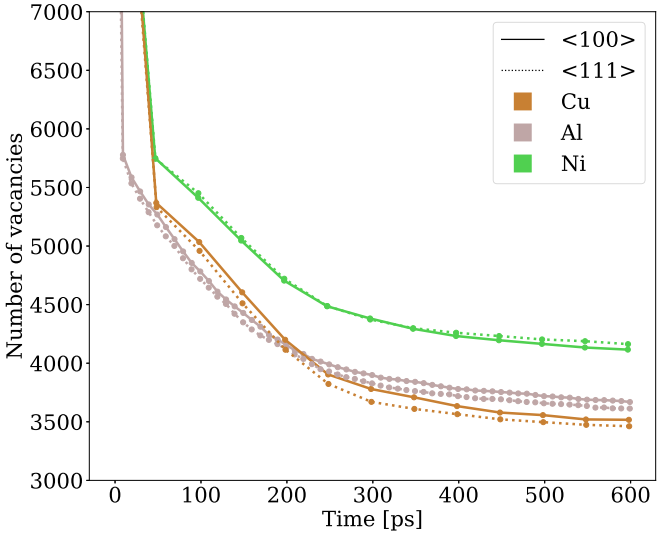

FIG. 8. Number of vacancies as a function of time during relaxation of inserted Frenkel pairs. The number of FPs in the initial configurations was on the order of 10 000. The two differently oriented simulation cells (⟨1 0 0⟩ and ⟨1 1 1⟩) are depicted. The simulation cells were heated up from 100 K to 300 K during the first 200 ps after which the temperature was maintained at 300 K for the rest of the simulation.

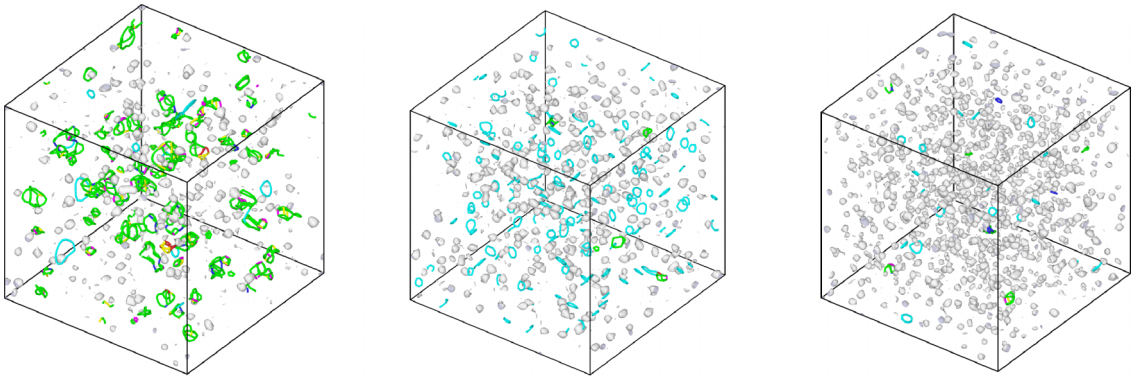

(a) Cu (b) Al (c) Ni

FIG. 9. Final dislocation structures after relaxation of Frenkel pair insertion. Green lines represent Shockley-partial dislocations, cyan lines represent Frank dislocations, pink lines represent stair-rod dislocations, and white blobs are defect clusters not identified as dislocations. The configurations depicted are the ⟨1 0 0⟩ lattice-oriented simulation cells.

using the conjugate gradient algorithm. During the following relaxation runs in the *NPT* ensemble, the vacancies and interstitials continue recombining but much slower until they reach a plateau at about 500 ps. The different saturation points seen are dependent on the defect structures formed during the relaxation. The final dislocation structures visualized using the DXA analysis in OVITO are shown in Fig. 9. It must be noted that we do not aim to compare the dislocation structure in different materials, since the final structures represent neither typical dislocation structures induced by irradiation nor those from simulations of overlapping cascades. Recently, it has been demonstrated that there are significant differences in the structure of defects created via FP insertion method and in radiation damage simulations [97]. Nevertheless, the FP insertion simulations give insight into the type of dislocations preferred by different potentials. From our results we clearly see that Frank loops are the preferred dislocations in Al, while in Cu Shockley partial dislocations dominate. In Ni we see both types of dislocations, but most of the defects are in clusters where no dislocation structure can be identified. From the FP insertion simulations we conclude that a saturated simulation cell has approximately a 0.004% vacancy concentration and we will use these structures in the compression simulations.

H. Uniaxial compressive loading

The stress-strain responses of Cu, Al and Ni using the tabGAP potentials during compression are shown in Fig. 10. Additionally, some selected pristine cells were simulated with EAM potentials as a reference. The strain in the figures are defined as the change in length of the simulation cell in the loading direction compared to the initial length. During loading, the stress in the system builds up until the system yields after which the stress drops to a low value of the flow stress. In general, there is a clear order in ranking of materials with respect to the yield stress (in this case defined as the maximal stress before the sudden drop): Ni has the highest and Al the lowest values of the yield stress in pristine cells. As an exception, we observe the lowest yield stress in the ⟨1 0 0⟩ loading direction for Cu. The order which we observe in our simulations is the same as that in the experimental equation of state and is in line with the known properties of the materials such as the Young's modulus of the respective materials. Overall, the yield stresses in the pristine cells in Fig. 10 are in good agreement with the values reported in previous MD studies of uniaxial compression [14,16,98]. However, in the case of Ni there is a significant difference between tabGAP and the classical EAM potentials, where there is a surprisingly wide spread in the predicted yield stresses [see Fig. 10(a); the different potentials in the legend are shown as Ni subscripts]. Additionally, the Mishin *et al.* potential for Ni shows irregular stress response in the ⟨1 0 0⟩ direction compared to the other Ni potentials and predicts significantly higher flow stress in the ⟨1 0 0⟩ case than the others. This irregular shape can also be seen in work on nanopillar compression, where the same EAM potential was used [99]. For the other elements there are no significant differences between tabGAP and the Mishin *et al.* EAM potentials with regards to the stress-strain relation, other than the strain at which the yield occurs. For all materials, we observe elastic hardening in the ⟨1 1 0⟩ direction and softening in ⟨1 0 0⟩ [compare in Fig. 10(b) and Fig. 10(a), where the peak sharpens or becomes blunt because of straining right before the yield point]. This is a known effect and has been reported previously [15,98]. In reality, some defects always exist that can act as nucleation sites for dislocations, thus the pristine cases are in practice artificial. In comparison, the systems containing defects (the cells relaxed after the Frenkel pair insertion) yielded with significantly lower strain and with a lower yield stress, at a value between 17 and 12 of the pristine cells. This is expected, as preexisting defects serve as nucleation sites for heterogeneous dislocation nucleation, which takes place at lower stresses than the homogeneous dislocation nucleation in the pristine cases. Before yielding the stress-strain curves of the cells with defective structures follow closely their pristine counterparts. Additionally, there are no significant differences in the flow stress between the damaged and pristine cells.

Figures 11, 12, and 13 show the dislocation structures identified by DXA analysis of the cells with all pristine materials and loading directions simulated with the tabGAP potentials. The figures show both the dislocation structures shortly after

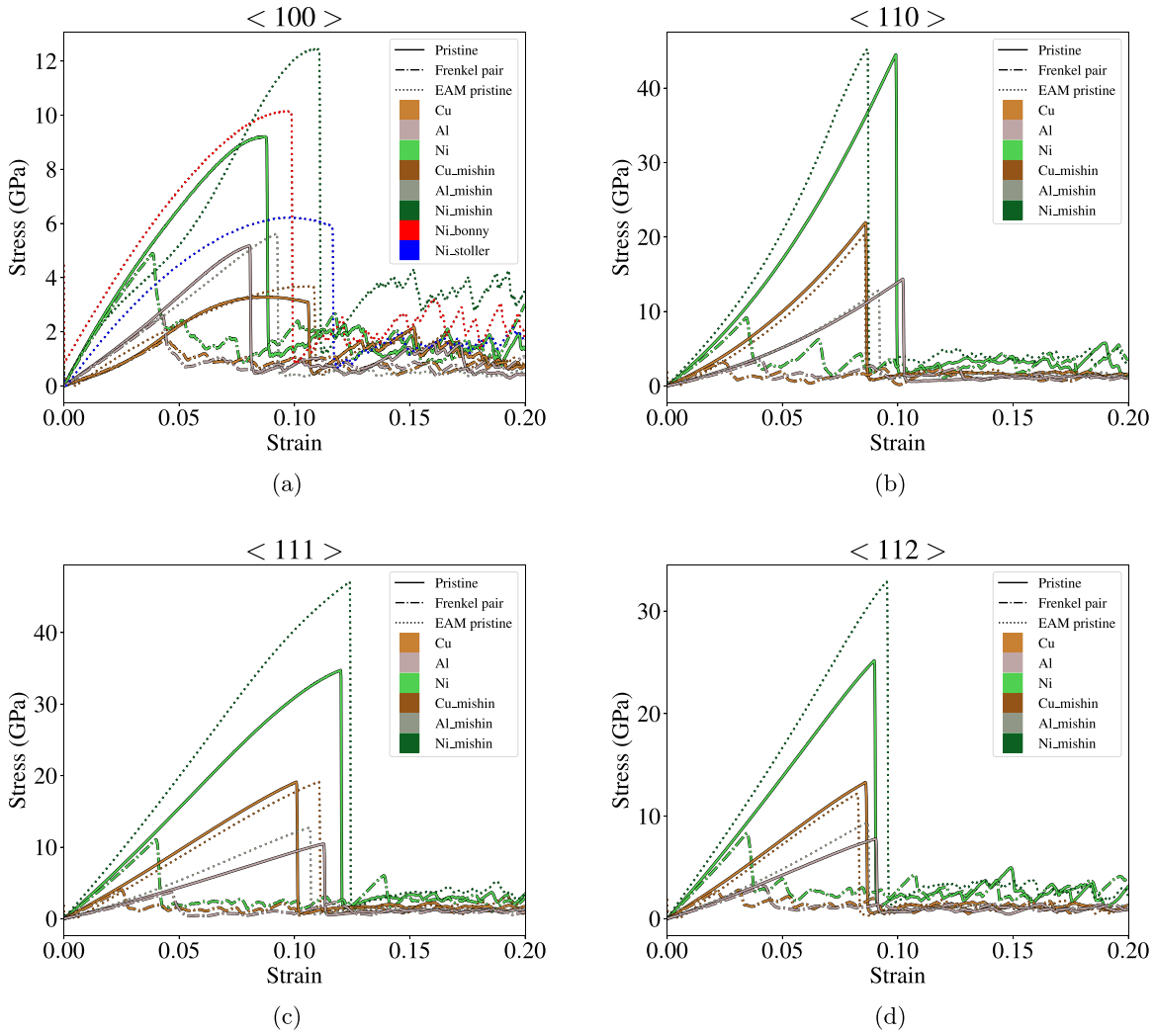

FIG. 10. Stress-strain curves during uniaxial compressive loading in different loading direction for different elements simulated with both tabGAP and EAM potentials. The simulation cells containing defects are here referred as Frenkel pair systems. The results are from simulations done using tabGAP potentials and EAM potentials [42–45].

yielding and the final structures at 20% strain. We see that shortly after yielding there is a complex dislocation network that mostly consists of Shockley-partial dislocation segments with some stair-rod-type dislocations. During continued compression, the dislocation network sparsifies, and at the end of the simulations there are fewer dislocations, but they span the whole simulation cell. In addition, stacking-fault tetrahedra (SFTs) can be observed for all materials, although fewer SFTs are found in Al. Furthermore, we also find considerably fewer SFTs in all materials during the compression in the ⟨1 0 0⟩ loading direction.

The ⟨1 0 0⟩ loading direction in Cu falls out from the general trend that we observe in our simulations. To clarify the reason for this behavior, we plot in Fig. 14 the resulting atomic structures of the Cu pristine cells after the loading in the ⟨1 0 0⟩ and ⟨1 1 1⟩ directions [Figs. 14(a) and 14(d), respectively] along with the dislocations as identified by the DXA in Figs. 14(b) and 14(e). We color the dislocations according to their type, i.e., the screw dislocations are shown in red and the edge ones in blue.

We see in the Cu cell deformed with the loading in the ⟨1 0 0⟩ direction a family of parallel stacking faults has formed, while loading in the ⟨1 1 1⟩ (or any other) direction does not cause similar cascade of the slips parallel to one another. Furthermore analyzing the dislocation structures, we observe that in the cell deformed in the ⟨1 0 0⟩ loading direction only the edge-type dislocations are present. In the cell deformed in the ⟨1 1 1⟩ loading direction we observe the mixture of both edge- and screw-type dislocations. For the other elements and loading directions we see a mixture of screw- and edge-type dislocations, similar to that in the Cu deformed in the ⟨1 1 1⟩ loading direction, but the ratio between the two types varies. Additionally, during compression no SFTs were identified in Cu for the ⟨1 0 0⟩ direction. The dislocation structure of the Cu cell during the ⟨1 0 0⟩ loading was not an artefact of the potential, since similar structures have developed in the cells simulated with the EAM potential [Figs. 14(c) and 14(f)]. Comparing against the EAM potential we can see that the structures are qualitatively similar. Furthermore, in Ni simulated with the EAM potentials the dislocation

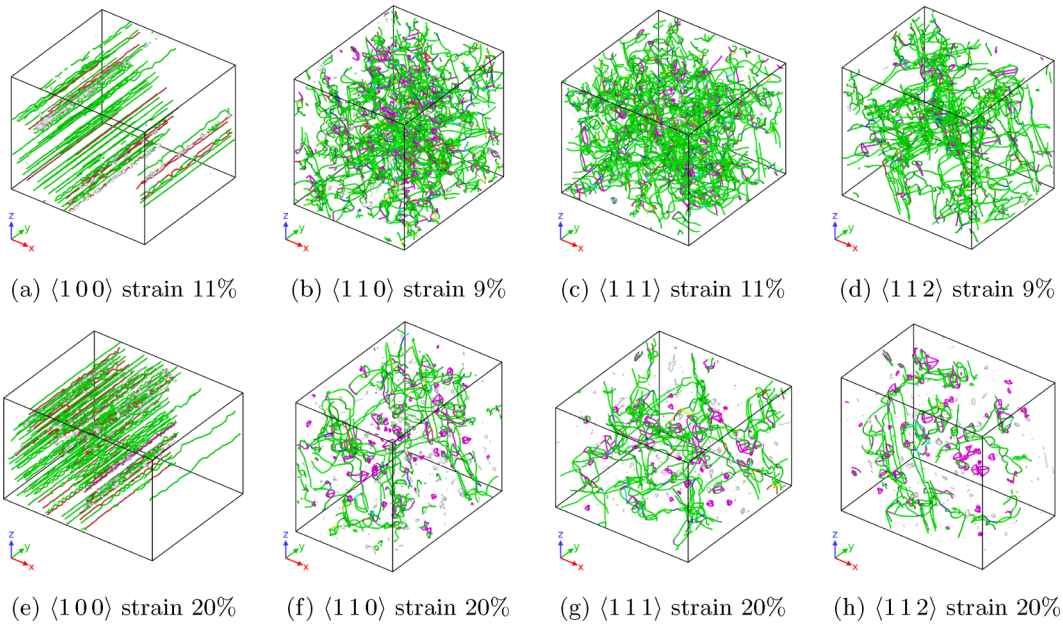

(a) ⟨1 0 0⟩ strain 11% (b) ⟨1 1 0⟩ strain 9% (c) ⟨1 1 1⟩ strain 11% (d) ⟨1 1 2⟩ strain 9%

(e) ⟨1 0 0⟩ strain 20% (f) ⟨1 1 0⟩ strain 20% (g) ⟨1 1 1⟩ strain 20% (h) ⟨1 1 2⟩ strain 20%

FIG. 11. Dislocation structures in Cu during compression in different loading directions with pristine cells. First row is immediately after yielding, and second row is the final configuration. Green lines represent Shockley partial dislocations, cyan lines represent Frank dislocations, pink lines represent stair-rod dislocations, and white blobs are defect clusters not identified as dislocations.

structures are formed similar to those in the Cu cells deformed in the ⟨1 0 0⟩ loading direction.

Figure 15 demonstrates the evolution of dislocation structures under compression in the ⟨1 1 1⟩ loading direction of the defected Al as relaxed after the random insertion of FPs. We see that at early stages of compression, small dislocations start nucleating at the preexisting defects in the system. The longer dislocations connecting the small initially disconnected ones appear at the strain of 4.7%, after which the dislocation network first grows denser and more connected, and then the initial smaller dislocations start fusing forming larger dislocation structures. Eventually, we observe formation of the dislocation network which is rather similar to that formed at deformation of the cell with the pristine structure. The dislocation networks grown in the cells during the loading in other directions as well as in the remaining materials with

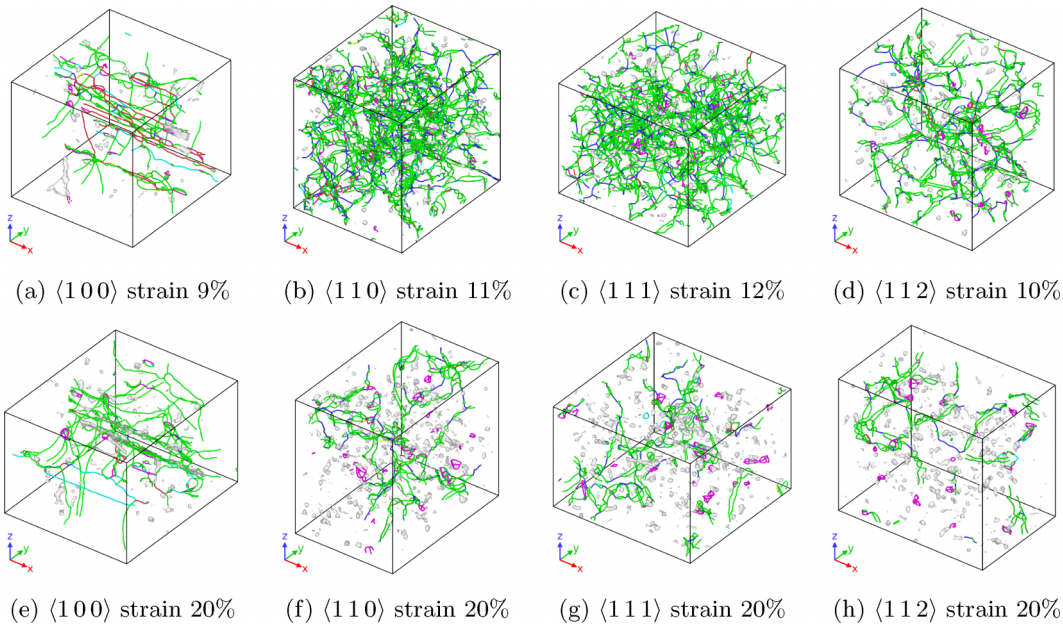

(a) ⟨1 0 0⟩ strain 9% (b) ⟨1 1 0⟩ strain 11% (c) ⟨1 1 1⟩ strain 12% (d) ⟨1 1 2⟩ strain 10%

(e) ⟨1 0 0⟩ strain 20% (f) ⟨1 1 0⟩ strain 20% (g) ⟨1 1 1⟩ strain 20% (h) ⟨1 1 2⟩ strain 20%

FIG. 12. Dislocation structures in Al during compression in different loading directions with pristine cells. First row is directly after yielding, and second row is the final configuration. Green lines represent Shockley partial dislocations, cyan lines represent Frank dislocations, pink lines represent stair-rod dislocations, and white blobs are defect clusters not identified as dislocations.

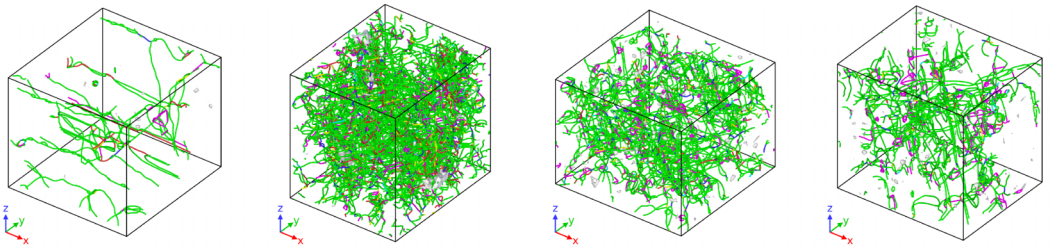

(a) ⟨1 0 0⟩ strain 10% (b) ⟨1 1 0⟩ strain 10% (c) ⟨1 1 1⟩ strain 13% (d) ⟨1 1 2⟩ strain 10%

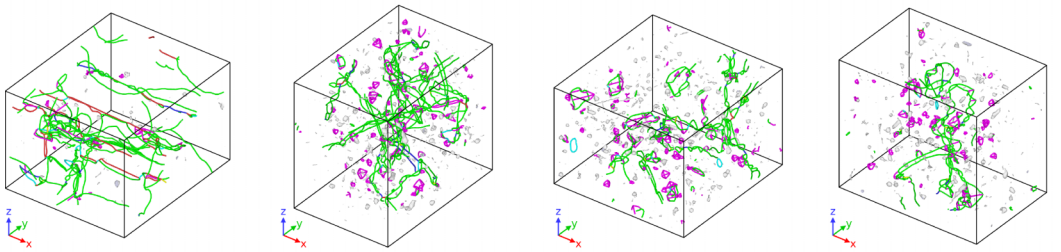

(e) ⟨1 0 0⟩ strain 20% (f) ⟨1 1 0⟩ strain 20% (g) ⟨1 1 1⟩ strain 20% (h) ⟨1 1 2⟩ strain 20%

FIG. 13. Dislocation structures in Ni during compression in different loading directions with pristine cells. First row is directly after yielding, and second row is the final configuration. Green lines represent Shockley partial dislocations, cyan lines represent Frank dislocations, pink lines represent stair-rod dislocations, and white blobs are defect clusters not identified as dislocations.

the predamaged structures can be found in the Supplemental Material [56].

In Fig. 16 we analyze the dislocation densities in all three materials in different loading directions. In most cases, the total dislocation density at the end of the compression is higher for the pristine structures. Furthermore, in pristine materials the total dislocation density rises rapidly reaching the peak at the yielding point. After that the total density

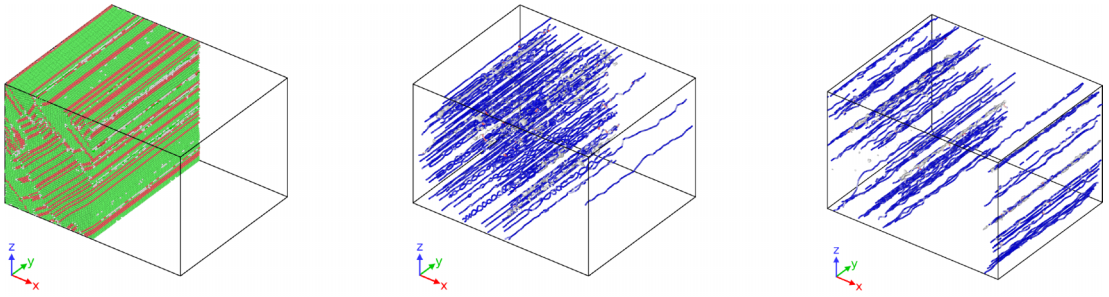

(a) ⟨1 0 0⟩ (b) ⟨1 0 0⟩ (c) ⟨1 0 0⟩ EAM

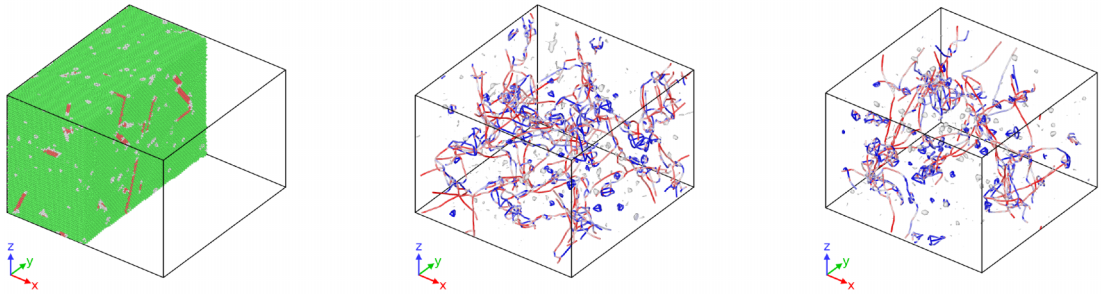

(d) ⟨1 1 1⟩ (e) ⟨1 1 1⟩ (f) ⟨1 1 1⟩ EAM

FIG. 14. Panels (a) and (d) show the atomistic structure of Cu in ⟨1 0 0⟩ and ⟨1 1 1⟩ loading directions at the final strain of 20%. The coloring of the atoms indicate lattice type of the atom based on common neighbor analysis. Green atoms are FCC, red atoms are HCP, and white atoms are without defined lattice structure. Half of the atoms are cut away in order to get a better view of the internal structure. Panels (b) and (e) show the corresponding dislocation structure with screw-type dislocations shown in red and edge type in blue. Panels (c) and (f) show the final dislocation structure like in (b) and (e) but using the Cu EAM potential [42].

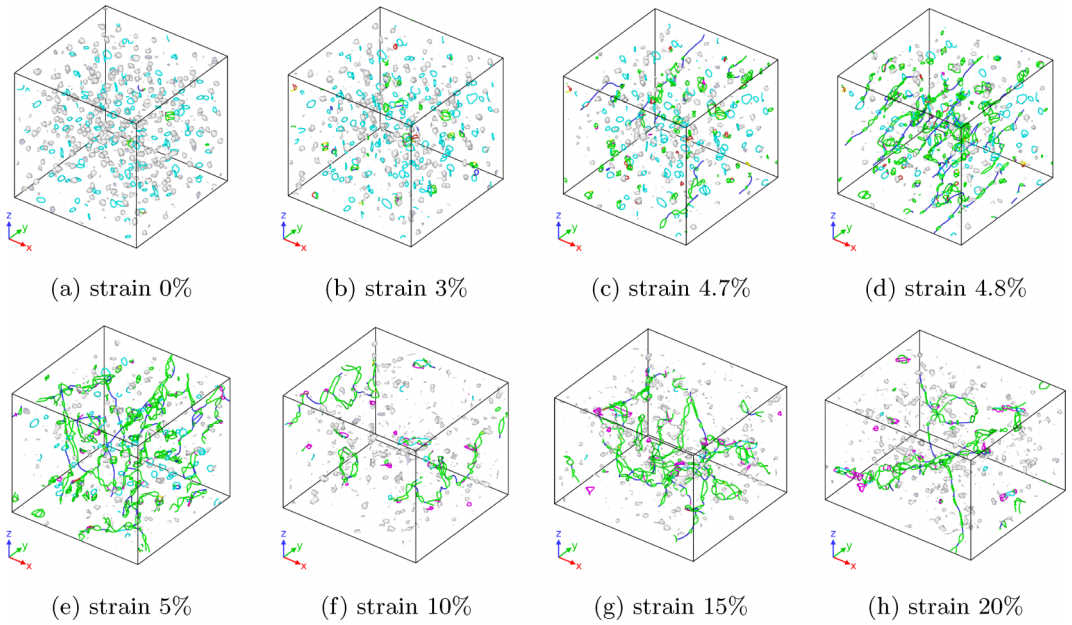

FIG. 15. Al cells containing preexisting defects from Frenkel pair insertion during compression in ⟨1 1 1⟩ loading direction. Green lines represent Shockley partial dislocations, cyan lines represent Frank dislocations, pink lines represent stair-rod dislocations, and white blobs are defect clusters not identified as dislocations.

first drops significantly, but then decrease of the density slows down reaching a steady state value. The dislocation densities reported here are of similar order of magnitude as those reported in the MD study in tantalum [17]. It should be noted that these dislocation densities are orders of magnitude higher than those typically reported in the experimental literature [100–104], due to the extreme strain rates in MD. The MD conditions are closer to those found in shock compression experiments, where higher dislocation densities are possible [105–107]. Recently, a model has been proposed that links strain rate, dislocation density, and yield stress, which could be used to bridge the gap between MD and experiments [108]. Although there is a large difference in the total dislocation densities after yielding between the cells with the initially pristine and damaged structures, under the continued compression the dislocation density converges to the same steady-state values in all loading directions, except for the ⟨1 0 0⟩ one. The path independence and loss of microstructure history has been also demonstrated during the simulation of compression in BCC materials (tantalum) [17]. This suggests that in most cases one could not determine from the final structure whether the initial one contained defects. Neither it is possible to do when analyzing the type of dislocations present in the metal after yielding. We note that the main difference appears in the density of stair-rod dislocations, which is significantly higher in the initially pristine cell.

In the ⟨1 0 0⟩ direction, on the other hand, there is a clear difference between the damaged and pristine structures, especially for Cu. This is due to the different dislocation types as is shown in Fig. 14 with different loading directions in Cu. Looking at the Frank dislocation densities we can observe that in all cases they are very low. A curious detail is that in some cases the EAM potentials show somewhat higher Frank-type dislocation densities in Al and Ni. Additionally, comparing the tabGAP to EAM potentials we can generally conclude that EAM potentials have higher dislocation densities during compression, with the results of Cu being closest to its tabGAP counterpart.

IV. CONCLUSIONS

We have developed machine-learned interatomic potentials for Al, Cu and Ni using the Gaussian approximation potential method. Fast and accurate tabGAP versions were created and extensively tested. The tabGAPs show similar accuracy as their GAP counterparts, while being orders of magnitude more computationally efficient, enabling large-scale simulations containing millions of atoms. The potentials were validated and are in good agreement with DFT calculations and experimental data for various material properties. Using the developed potentials, we simulate the threshold displacement energies as a function of lattice direction for each of the elements. In addition to this, uniaxial compression simulations were performed on both pristine simulation cells and cells containing preexisting defects. The stress strain curves for the pristine cases were in agreement with what has been reported previously. However, in Ni we could see large differences between different interatomic potentials. The compression simulations demonstrate the feasibility to simulate large-scale systems on the order of millions of atoms with the machine-learned tabGAPs. Furthermore, the diverse DFT databases for the training of the potentials can be augmented and used for future work on alloys.

ACKNOWLEDGMENTS

This work has received funding from Research Council of Finland through the HEADFORE project (Grant No. 333225). The authors wish to thank the Finnish Computing Competence Infrastructure (FCCI) and CSC–IT Center for

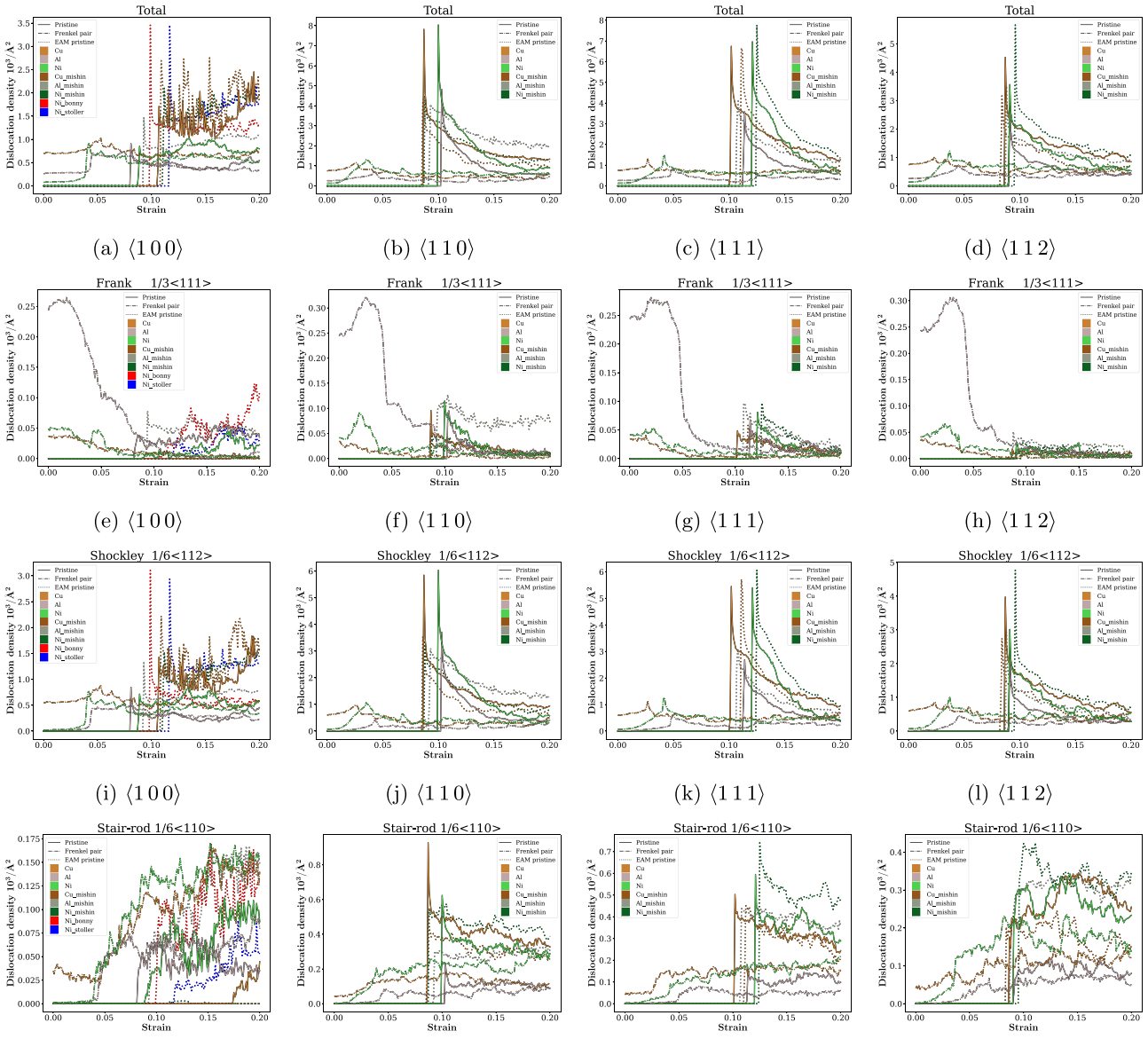

FIG. 16. Dislocation density as a function of strain for various types of dislocations (rows) and different loading directions (columns). The dislocation types are shown in the caption of the individual panels: "Total" includes all types of dislocations found in the structures; "Frank $1/3\langle 1\,1\,1\rangle$," "Shockley $1/6\langle 1\,1\,2\rangle$," and "Stair-rod $1/6\langle 1\,1\,2\rangle$" refer to the corresponding dislocation types. The loading directions $\langle 1\,0\,0\rangle$, $\langle 1\,1\,0\rangle$, $\langle 1\,1\,1\rangle$, and $\langle 1\,1\,2\rangle$ for each case are given under the corresponding panels. Pristine refers to the cells with no preexisting defects, and Frenkel pair refers to the cells relaxed after insertion of Frenkel pairs. Results from simulations with the developed tabGAP potentials and EAM potentials in the literature [42–45].

Science for supporting this project with computational and data storage resources. This work has been partially carried out within the framework of the EUROfusion Consortium, funded by the European Union via the Euratom Research and Training Programme (Grant Agreement No. 101052200—EUROfusion). Views and opinions expressed are, however, those of the authors only and do not necessarily reflect those of the European Union or the European Commission. Neither the European Union nor the European Commission can be held responsible for them.

[1] A. P. Bartók, J. Kermode, N. Bernstein, and G. Csányi, Machine learning a general-purpose interatomic potential for silicon, Phys. Rev. X **8**, 041048 (2018).

[2] V. L. Deringer and G. Csányi, Machine learning based interatomic potential for amorphous carbon, Phys. Rev. B **95**, 094203 (2017).

[3] G. P. Pun, V. Yamakov, J. Hickman, E. H. Glaessgen, and Y. Mishin, Development of a general-purpose machine-learning interatomic potential for aluminum by the physically informed neural network method, Phys. Rev. Mater. **4**, 113807 (2020).

[4] Y. Zuo, C. Chen, X. Li, Z. Deng, Y. Chen, J. Behler, G. Csányi, A. V. Shapeev, A. P. Thompson, M. A. Wood, and S. P. Ong, Performance and cost assessment of machine learning interatomic potentials, J. Phys. Chem. A **124**, 731 (2020).

[5] Y. Lysogorskiy, C. van der Oord, A. Bochkarev, S. Menon, M. Rinaldi, T. Hammerschmidt, M. Mrovec, A. Thompson, G. Csányi, C. Ortner *et al.*, Performant implementation of the atomic cluster expansion (PACE) and application to copper and silicon, npj Comput. Mater. **7**, 97 (2021).

[6] N. Lopanitsyna, C. Ben Mahmoud, and M. Ceriotti, Finite-temperature materials modeling from the quantum nuclei to the hot electron regime, Phys. Rev. Mater. **5**, 043802 (2021).

[7] K. Song, R. Zhao, J. Liu, Y. Wang, E. Lindgren, Y. Wang, S. Chen, K. Xu, T. Liang, P. Ying *et al.*, General-purpose machine-learned potential for 16 elemental metals and their alloys, Nat. Commun. **15**, 10208 (2024).

[8] J. Byggmästar, A. Hamedani, K. Nordlund, and F. Djurabekova, Machine-learning interatomic potential for radiation damage and defects in tungsten, Phys. Rev. B **100**, 144105 (2019).

[9] D. Marchand, A. Jain, A. Glensk, and W. A. Curtin, Machine learning for metallurgy I. A neural-network potential for Al-Cu, Phys. Rev. Mater. **4**, 103601 (2020).

[10] A. C. Lund, T. G. Nieh, and C. A. Schuh, Tension/compression strength asymmetry in a simulated nanocrystalline metal, Phys. Rev. B **69**, 012101 (2004).

[11] D. Spearot, M. Tschopp, and D. McDowell, Orientation and rate dependence of dislocation nucleation stress computed using molecular dynamics, Scr. Mater. **60**, 675 (2009).

[12] M. Tschopp, D. Spearot, and D. McDowell, Atomistic simulations of homogeneous dislocation nucleation in single crystal copper, Modell. Simul. Mater. Sci. Eng. **15**, 693 (2007).

[13] M. A. Tschopp and D. L. McDowell, Tension-compression asymmetry in homogeneous dislocation nucleation in single crystal copper, Appl. Phys. Lett. **90**, 121916 (2007).

[14] Z. Li, Y. Gao, S. Zhan, H. Fang, and Z. Zhang, Molecular dynamics study on temperature and strain rate dependences of mechanical properties of single crystal Al under uniaxial loading, AIP Adv. **10**, 075321 (2020).

[15] L. Zhang, C. Lu, and A. K. Tieu, Nonlinear elastic response of single crystal Cu under uniaxial loading by molecular dynamics study, Mater. Lett. **227**, 236 (2018).

[16] H. Xie, T. Yu, and F. Yin, Tension–compression asymmetry in homogeneous dislocation nucleation stress of single crystals Cu, Au, Ni and Ni_3Al, Mater. Sci. Eng. A **604**, 142 (2014).

[17] L. A. Zepeda-Ruiz, A. Stukowski, T. Oppelstrup, and V. V. Bulatov, Probing the limits of metal plasticity with molecular dynamics simulations, Nature (London) **550**, 492 (2017).

[18] I. Salehinia and D. Bahr, Crystal orientation effect on dislocation nucleation and multiplication in FCC single crystal under uniaxial loading, Int. J. Plast. **52**, 133 (2014).

[19] L. Zhang, C. Lu, K. Tieu, L. Su, X. Zhao, and L. Pei, Stacking fault tetrahedron induced plasticity in copper single crystal, Mater. Sci. Eng. A **680**, 27 (2017).

[20] J. Hu, X. Ye, X. Liu, and Z. Chen, The effects of initial void and dislocation on the onset of plasticity in copper single crystals, J. Appl. Phys. **126**, 165104 (2019).

[21] B. Tang and R. Yang, Molecular dynamics study of uniaxial deformation in perfect and defective aluminum, Chin. J. Phys **53**, 120802 (2015).

[22] J. Wang, Z. Yue, Z. Wen, D. Zhang, and C. Liu, Orientation effects on the tensile properties of single crystal nickel with nanovoid: Atomistic simulation, Comput. Mater. Sci. **132**, 116 (2017).

[23] T. Zhu, J. Li, K. J. Van Vliet, S. Ogata, S. Yip, and S. Suresh, Predictive modeling of nanoindentation-induced homogeneous dislocation nucleation in copper, J. Mech. Phys. Solids **52**, 691 (2004).

[24] A. P. Bartók, M. C. Payne, R. Kondor, and G. Csányi, Gaussian approximation potentials: The accuracy of quantum mechanics, without the electrons, Phys. Rev. Lett. **104**, 136403 (2010).

[25] J. F. Ziegler, J. P. Biersack, and U. Littmarck, The stopping and range of ions in matter, *Treatise on Heavy-Ion Science* (Pergamon, New York, 1985), pp. 93–129.

[26] K. Nordlund, N. Runeberg, and D. Sundholm, Repulsive interatomic potentials calculated using Hartree-Fock and density-functional theory methods, Nucl. Instrum. Methods Phys. Res. B **132**, 45 (1997).

[27] A. P. Bartók, R. Kondor, and G. Csányi, On representing chemical environments, Phys. Rev. B **87**, 184115 (2013).

[28] J. Byggmästar, K. Nordlund, and F. Djurabekova, Simple machine-learned interatomic potentials for complex alloys, Phys. Rev. Mater. **6**, 083801 (2022).

[29] J. Byggmästar, G. Nikoulis, A. Fellman, F. Granberg, F. Djurabekova, and K. Nordlund, Multiscale machine-learning interatomic potentials for ferromagnetic and liquid iron, J. Phys.: Condens. Matter **34**, 305402 (2022).

[30] A. P. Bartók and G. Csányi, Gaussian approximation potentials: A brief tutorial introduction, Int. J. Quantum Chem. **115**, 1051 (2015).

[31] M. S. Daw and M. I. Baskes, Embedded-atom method: Derivation and application to impurities, surfaces, and other defects in metals, Phys. Rev. B **29**, 6443 (1984).

[32] M. W. Finnis and J. E. Sinclair, A simple empirical *N*-body potential for transition metals, Philos. Mag. A **50**, 45 (1984).

[33] J. Byggmästar, K. Nordlund, and F. Djurabekova, Modeling refractory high-entropy alloys with efficient machine-learned interatomic potentials: Defects and segregation, Phys. Rev. B **104**, 104101 (2021).

[34] G. Kresse and J. Hafner, *Ab initio* molecular dynamics for liquid metals, Phys. Rev. B **47**, 558 (1993).

[35] G. Kresse and J. Hafner, *Ab initio* molecular-dynamics simulation of the liquid-metal–amorphous-semiconductor transition in germanium, Phys. Rev. B **49**, 14251 (1994).

[36] G. Kresse and J. Furthmüller, Efficiency of ab-initio total energy calculations for metals and semiconductors using a plane-wave basis set, Comput. Mater. Sci. **6**, 15 (1996).

[37] G. Kresse and J. Furthmüller, Efficient iterative schemes for *ab initio* total-energy calculations using a plane-wave basis set, Phys. Rev. B **54**, 11169 (1996).

[38] J. P. Perdew, K. Burke, and M. Ernzerhof, Generalized gradient approximation made simple, Phys. Rev. Lett. **77**, 3865 (1996).

[39] H. J. Monkhorst and J. D. Pack, Special points for Brillouin-zone integrations, Phys. Rev. B **13**, 5188 (1976).

[40] M. Methfessel and A. T. Paxton, High-precision sampling for Brillouin-zone integration in metals, Phys. Rev. B **40**, 3616 (1989).

[41] A. P. Thompson, H. M. Aktulga, R. Berger, D. S. Bolintineanu, W. M. Brown, P. S. Crozier, P. J. in 't Veld, A. Kohlmeyer, S. G. Moore, T. D. Nguyen *et al.*, LAMMPS—A flexible simulation tool for particle-based materials modeling at the atomic, meso, and continuum scales, Comput. Phys. Commun. **271**, 108171 (2022).

[42] Y. Mishin, M. Mehl, D. Papaconstantopoulos, A. Voter, and J. Kress, Structural stability and lattice defects in copper: *Ab initio*, tight-binding, and embedded-atom calculations, Phys. Rev. B **63**, 224106 (2001).

[43] Y. Mishin, D. Farkas, M. J. Mehl, and D. A. Papaconstantopoulos, Interatomic potentials for monoatomic metals from experimental data and *ab initio* calculations, Phys. Rev. B **59**, 3393 (1999).

[44] R. Stoller, A. Tamm, L. Béland, G. Samolyuk, G. Stocks, A. Caro, L. Slipchenko, Y. N. Osetsky, A. Aabloo, M. Klintenberg *et al.*, Impact of short-range forces on defect production from high-energy collisions, J. Chem. Theory Comput. **12**, 2871 (2016).

[45] G. Bonny, N. Castin, and D. Terentyev, Interatomic potential for studying ageing under irradiation in stainless steels: The FeNiCr model alloy, Modell. Simul. Mater. Sci. Eng. **21**, 085004 (2013).

[46] R. Tran, Z. Xu, B. Radhakrishnan, D. Winston, W. Sun, K. A. Persson, and S. P. Ong, Surface energies of elemental crystals, Sci. Data **3**, 160080 (2016).

[47] V. Kumikov and K. B. Khokonov, On the measurement of surface free energy and surface tension of solid metals, J. Appl. Phys. **54**, 1346 (1983).

[48] J. R. Morris, C. Z. Wang, K. M. Ho, and C. T. Chan, Melting line of aluminum from simulations of coexisting phases, Phys. Rev. B **49**, 3109 (1994).

[49] W. M. Haynes, *CRC Handbook of Chemistry and Physics*, 96th ed. (CRC Press, Boca Raton, FL, 2015).

[50] P.-W. Ma and S. L. Dudarev, Nonuniversal structure of point defects in face-centered cubic metals, Phys. Rev. Mater. **5**, 013601 (2021).

[51] C. Kittel, *Introduction to Solid State Physics*, 3rd ed. (John Wiley & Sons, New York, 1968).

[52] P. Ehrhart, Atomic defects in metals ċ Cu datasheet from Landolt-Börnstein - Group III condensed matter, in *Atomic Defects in Metals*, Springer Materials Vol. 25, edited by H. Ullmaier (Springer-Verlag, Berlin, Heidelberg, 1991).

[53] P. Ehrhart, Atomic defects in metals ċ Al datasheet from Landolt-Börnstein - Group III condensed matter, in *Atomic Defects in Metals*, Springer Materials Vol. 25, edited by H. Ullmaier (Springer-Verlag, Berlin, Heidelberg, 1991).

[54] P. Ehrhart, Atomic defects in metals ċ Ni datasheet from Landolt-Börnstein - Group III condensed matter, in *Atomic Defects in Metals*, Springer Materials Vol. 25 edited by H. Ullmaier (Springer-Verlag, Berlin, Heidelberg, 1991).

[55] R. Qiu, H. Lu, B. Ao, L. Huang, T. Tang, and P. Chen, Energetics of intrinsic point defects in aluminium via orbital-free density functional theory, Philos. Mag. **97**, 2164 (2017).

[56] See Supplemental Material at http://link.aps.org/supplemental/10.1103/PhysRevMaterials.9.053807 for the BCC and HCP volume energy curves, nondissosiated screw dislocation in Al for the tabGAP potential, and visualizations of the dislocation structures of the uniaxial compressive loading in predamaged Cu, Al, and Ni.

[57] A. M. Goryaeva, C. Domain, A. Chartier, A. Dézaphie, T. D. Swinburne, K. Ma, M. Loyer-Prost, J. Creuze, and M.-C. Marinica, Compact A15 Frank-Kasper nano-phases at the origin of dislocation loops in face-centred cubic metals, Nat. Commun. **14**, 3003 (2023).

[58] T. Jourdan, A. M. Goryaeva, and M.-C. Marinica, Preferential nucleation of dislocation loops under stress explained by A15 Frank-Kasper nanophases in aluminum, Phys. Rev. Lett. **132**, 226101 (2024).

[59] G. Nilsson and S. Rolandson, Lattice dynamics of copper at 80 K, Phys. Rev. B **7**, 2393 (1973).

[60] R. t. Stedman and G. Nilsson, Dispersion relations for phonons in aluminum at 80 and 300 K, Phys. Rev. **145**, 492 (1966).

[61] G. A. deWit and B. Brockhouse, The lattice dynamics of ferromagnetic and paramagnetic nickel, J. Appl. Phys. **39**, 451 (1968).

[62] A. Hunter, R. Zhang, and I. Beyerlein, The core structure of dislocations and their relationship to the material γ-surface, J. Appl. Phys. **115**, 134314 (2014).

[63] S. Ogata, J. Li, and S. Yip, Ideal pure shear strength of aluminum and copper, Science **298**, 807 (2002).

[64] M. Jahnátek, J. Hafner, and M. Krajčí, Shear deformation, ideal strength, and stacking fault formation of fcc metals: A density-functional study of Al and Cu, Phys. Rev. B **79**, 224103 (2009).

[65] C. Carter and I. Ray, On the stacking-fault energies of copper alloys, Philos. Mag. **35**, 189 (1977).

[66] R. Rautioaho, An interatomic pair potential for aluminium calculation of stacking fault energy, Phys. Status Solidi B **112**, 83 (1982).

[67] M. J. Mills and P. Stadelmann, A study of the structure of lomer and 60 dislocations in aluminium using high-resolution transmission electron microscopy, Philos. Mag. A **60**, 355 (1989).

[68] P. M. Anderson, J. P. Hirth, and J. Lothe, *Theory of Dislocations* (Cambridge University Press, Cambridge, 2017).

[69] W. Stobbs and C. Sworn, The weak beam technique as applied to the determination of the stacking-fault energy of copper, Philos. Mag. **24**, 1365 (1971).

[70] C. Brandl, P. M. Derlet, and H. Van Swygenhoven, General-stacking-fault energies in highly strained metallic environments: *Ab initio* calculations, Phys. Rev. B **76**, 054124 (2007).

[71] Y. Hu, B. Szajewski, D. Rodney, and W. Curtin, Atomistic dislocation core energies and calibration of non-singular discrete dislocation dynamics, Modell. Simul. Mater. Sci. Eng. **28**, 015005 (2020).

[72] D. Rodney, L. Ventelon, E. Clouet, L. Pizzagalli, and F. Willaime, Ab initio modeling of dislocation core properties in metals and semiconductors, Acta Mater. **124**, 633 (2017).

[73] C. Woodward, D. R. Trinkle, L. G. Hector, Jr., and D. L. Olmsted, Prediction of dislocation cores in aluminum from density functional theory, Phys. Rev. Lett. **100**, 045507 (2008).

[74] A. M. Z. Tan, C. Woodward, and D. R. Trinkle, Dislocation core structures in Ni-based superalloys computed using a density functional theory based flexible boundary condition approach, Phys. Rev. Mater. **3**, 033609 (2019).

[75] I. Shin and E. A. Carter, Possible origin of the discrepancy in peierls stresses of fcc metals: First-principles simulations of dislocation mobility in aluminum, Phys. Rev. B **88**, 064106 (2013).

[76] A. Stukowski and K. Albe, Extracting dislocations and non-dislocation crystal defects from atomistic simulation data, Modell. Simul. Mater. Sci. Eng. **18**, 085001 (2010).

[77] F. Deng, H. Wu, R. He, P. Yang, and Z. Zhong, Large-scale atomistic simulation of dislocation core structure in face-centered cubic metal with deep potential method, Comput. Mater. Sci. **218**, 111941 (2023).

[78] L. Mismetti and M. Hodapp, Automated atomistic simulations of dissociated dislocations with *ab initio* accuracy, Phys. Rev. B **109**, 094120 (2024).

[79] M. Iyer, B. Radhakrishnan, and V. Gavini, Electronic-structure study of an edge dislocation in aluminum and the role of macroscopic deformations on its energetics, J. Mech. Phys. Solids **76**, 260 (2015).

[80] S. Das and V. Gavini, Electronic structure study of screw dislocation core energetics in aluminum and core energetics informed forces in a dislocation aggregate, J. Mech. Phys. Solids **104**, 115 (2017).

[81] X. Gong, Z. Li, A. S. Pattamatta, T. Wen, and D. J. Srolovitz, An accurate and transferable machine learning interatomic potential for nickel, Commun. Mater. **5**, 157 (2024).

[82] V. N. Antonov, V. Y. Milman, V. V. Nemoshkalenko, and A. V. Zhalko-Titarenko, Equation of state and thermodynamics of fcc transition metals: A pseudopotential approach, Z. Phys. B **79**, 233 (1990).

[83] A. Dewaele, P. Loubeyre, and M. Mezouar, Equations of state of six metals above 94 GPa, Phys. Rev. B **70**, 094112 (2004).

[84] M. Rice, R. McQueen, and J. Walsh, Compression of solids by strong shock waves, in *Advances in Research and Applications*, edited by F. Seitz and D. Turnbull, Solid State Physics, Vol. 6 (Academic Press, San Diego, 1958), pp. 1–63.

[85] L. Al'Tshuler, A. Bakanova, and R. Trunin, Shock adiabats and zero isotherms of seven metals at high pressures, Sov. Phys. JETP **15**, 65 (1962).

[86] K. Nordlund, S. J. Zinkle, A. E. Sand, F. Granberg, R. S. Averback, R. E. Stoller, T. Suzudo, L. Malerba, F. Banhart, W. J. Weber *et al.*, Primary radiation damage: A review of current understanding and models, J. Nucl. Mater. **512**, 450 (2018).

[87] K. Nordlund, S. J. Zinkle, A. E. Sand, F. Granberg, R. S. Averback, R. Stoller, T. Suzudo, L. Malerba, F. Banhart, W. J. Weber *et al.*, Improving atomic displacement and replacement calculations with physically realistic damage models, Nat. Commun. **9**, 1084 (2018).

[88] M. Norgett, M. Robinson, and I. Torrens, A proposed method of calculating displacement dose rates, Nucl. Eng. Des. **33**, 50 (1975).

[89] Q. Yang and P. Olsson, Full energy range primary radiation damage model, Phys. Rev. Mater. **5**, 073602 (2021).

[90] H. Wang, X. Guo, L. Zhang, H. Wang, and J. Xue, Deep learning inter-atomic potential model for accurate irradiation damage simulations, Appl. Phys. Lett. **114**, 244101 (2019).

[91] ASTM Standard E521-96, Standard practice for neutron radiation damage simulation by charged-particle irradiation (2009), https://doi.org/10.1520/E0521-96.

[92] P. Vajda, Anisotropy of electron radiation damage in metal crystals, Rev. Mod. Phys. **49**, 481 (1977).

[93] P. Jung, Average atomic-displacement energies of cubic metals, Phys. Rev. B **23**, 664 (1981).

[94] P. Lucasson, The production of Frenkel defects in metals, in *Fundamental Aspects of Radiation Damage in Metals*, edited by M. T. Robinson and F. N. Young Jr. (ORNL, Springfield, 1975), pp. 42–65.

[95] A. Stukowski, Visualization and analysis of atomistic simulation data with OVITO—The open visualization tool, Modelling Simul. Mater. Sci. Eng. **18**, 015012 (2010).

[96] A. Stukowski, V. V. Bulatov, and A. Arsenlis, Automated identification and indexing of dislocations in crystal interfaces, Modell. Simul. Mater. Sci. Eng. **20**, 085007 (2012).

[97] F. Granberg, D. Mason, and J. Byggmästar, Effect of simulation technique on the high-dose damage in tungsten, Comput. Mater. Sci. **217**, 111902 (2023).

[98] M. Tschopp and D. McDowell, Influence of single crystal orientation on homogeneous dislocation nucleation under uniaxial loading, J. Mech. Phys. Solids **56**, 1806 (2008).

[99] D. Zhang, X. Liu, T. Li, K. Fu, Z. Peng, and Y. Zhu, New insights of the strength asymmetry in fcc single-crystalline nanopillars, Comput. Mater. Sci. **208**, 111360 (2022).

[100] F. W. Young, Jr., On the yield stress of copper crystals, J. Appl. Phys. **33**, 963 (1962).

[101] J. D. Livingston, The density and distribution of dislocations in deformed copper crystals, Acta Metall. **10**, 229 (1962).

[102] J. Edington, The influence of strain rate on the mechanical properties and dislocation substructure in deformed copper single crystals, Philos. Mag. **19**, 1189 (1969).

[103] G. Van Drunen and S. Saimoto, Deformation and recovery of [001] oriented copper crystals, Acta Metall. **19**, 213 (1971).

[104] C. Chiem and J. Duffy, Strain rate history effects and observations of dislocation substructure in aluminum single crystals following dynamic deformation, Mater. Sci. Eng. **57**, 233 (1983).

[105] F. Greulich and L. Murr, Effect of grain size, dislocation cell size and deformation twin spacing on the residual strengthening of shock-loaded nickel, Mater. Sci. Eng. **39**, 81 (1979).

[106] M. A. Meyers, F. Gregori, B. Kad, M. Schneider, D. Kalantar, B. Remington, G. Ravichandran, T. Boehly, and J. Wark, Laser-induced shock compression of monocrystalline copper: Characterization and analysis, Acta Mater. **51**, 1211 (2003).

[107] W. Murphy, A. Higginbotham, G. Kimminau, B. Barbrel, E. M. Bringa, J. Hawreliak, R. Kodama, M. Koenig, W. McBarron, M. Meyers *et al.*, The strength of single crystal copper under uniaxial shock compression at 100 GPa, J. Phys.: Condens. Matter **22**, 065404 (2010).

[108] H. Fan, Q. Wang, J. A. El-Awady, D. Raabe, and M. Zaiser, Strain rate dependency of dislocation plasticity, Nat. Commun. **12**, 1845 (2021).